UNDERSTANDING THE ORIGIN AND PREDICTION OF LASER WELDING DEFECTS IN HIGHLY REFLECTIVE METALS: A NUMERICAL STUDY APPLIED TO A2219 ALLOY

B. F. CHETAN*,**[1], M. COURTOIS**, S. CADIOU**, M. CARIN**,
V. NAIN*, F. MACHI*, A. ALVES FERREIRA*

**IREPA LASER, Parc d'Innovation, 67400 Illkirch, France.*
***Univ. Bretagne Sud, UMR CNRS 6027, IRDL, F-56100 Lorient, France.*
[1]Corresponding author: fchetan@irepa-laser.com

DOI 10.3217/978-3-99161-089-2-007,

ABSTRACT

A new approach to modeling and simulating multiple reflections of a laser beam has been developed under COMSOL Multiphysics®. It is based on a special coupling between a modified ray tracing method and Level-set. Initial application results for laser welding on aluminum in static pulse and fusion line cases are compared with theory and experiments.

Keywords: heat transfer; fluid flow; laser welding; multiple reflections; reflective materials; Level-set; keyhole behavior

INTRODUCTION

Under certain operating conditions, laser welding is subject to undesirable phenomena such as melt instabilities and the formation of defects that affect the integrity of the welded parts. The difficulty of controlling these defects depends on the nature of the materials studied. This study focuses on materials such as aluminum, which are both reflective and good thermal conductors. Indeed, laser welding of aluminum in an industrial context (energy density $\gtrsim 1$ MW/cm^2, penetration $\gtrsim 1$ mm) is characterized by fluctuating keyholes and unstable melt flows. It results in beads potentially affected by defects (notably porosity defects) detrimental to the integrity of the welded parts.

Since the first experimental studies of keyhole dynamics using X-ray imaging by Matsunawa *et al* [1], [2], a link has been established between keyhole fluctuations and non-uniform irradiance distribution. This result was subsequently supported by numerical studies. These include Ke *et al* [3], who discuss keyhole stability and porosity reduction through beam oscillation, and Fetzer *et al* [4], who show that at low welding speeds, the keyhole is subject to strong fluctuations accompanied by significant variations in local irradiance, resulting in trapped gas bubbles and possibly residual porosities.

This shows that the correct representation of energy deposition is a fundamental aspect of the development of an accurate and predictive numerical model of laser welding. There are three approaches in the literature to model energy deposition: analytical, wave and geometrical approaches. The analytical approach, which consists of weighting the laser intensity by an absorptivity coefficient (constant or increasing with keyhole depth, according to Gouffé's formula [5]), does not allow the phenomenon of multiple reflections to be simulated, but only its global effect to be taken into account. The wave-based approach developed by Courtois *et al* [6] involves solving Maxwell's equations. This method was used to develop a 2D multiphysics model of the melt pool under static pulse conditions. The phenomenon of multiple reflections is well represented, and the model can reproduce experimentally observed porosities. However, the method is very demanding in terms of mesh refinement and therefore computation time and has never been used for 3D weld bead models. Finally, the geometrical approach known as Ray tracing, an intermediate solution between the two previous ones (less constraining than electromagnetism and more realistic than an analytical formula), consists of discretizing the beam into a finite number of rays to which the laws of geometrical optics are applied. This option has been used in recent studies on thermohydrodynamic simulation of laser welding: Daligault *et al* [7], Westhofen *et al* [8]. However, the use of Ray tracing is not as straightforward, as its algorithm is not integrated into commercial laser welding simulation software. Researchers are therefore obliged either to develop customized Ray tracing codes or software (e.g. the "in-house code" used in their work by Lind *et al* [9]), or to use the Java or Matlab extensions of commercial software to implement the algorithm for calculating multiple reflections (e.g. the work by Mayi *et al* [10]). In both cases, the digital tool developed becomes the property of the research team and is neither accessible nor exploitable by a third party.

In this study, we have developed a new method to describe laser-matter interaction, considering multiple beam reflections in the keyhole. The method is based on the theory of geometrical optics but differs from conventional Ray tracing in one fundamental respect: all couplings are performed using the same software (COMSOL Multiphysics®), without the need for any additional software (Matlab or Java environment). This ability to couple the thermohydrodynamic problem and the multiple beam reflections in a single computation code means simplicity of implementation, and a saving in calculation time. The physical coherence of the model has been proved. The aim of this paper is to present the first results of this new approach, for a better understanding of the origins of melt instabilities and porosity-type defects in aluminum welding.

DESCRIPTION OF LASER-MATTER INTERACTION

The new approach developed is based on a modified ray tracing method, in which the velocity of the rays is artificially reduced to ensure compatibility with solvers available in commercial Finite Element Method software. This approach is purely numerical and is intended solely to describe the laser beam trajectory inside the keyhole.

FUNDAMENTAL EQUATION

The motion of a ray is solved here by Newton's second law with assumption of straight-line propagation:

$$\frac{d}{dt}\left(\frac{d\vec{q}}{dt}\right) = \vec{0} \tag{1}$$

$$\frac{d\vec{q}}{dt} = \vec{V} \tag{2}$$

with $\vec{q}$ the ray’s position vector, and $\vec{V}$ its velocity vector.

MODELING MULTIPLE REFLECTIONS

Ray reflections at the free interface obey the Snell-Descartes laws:

$$\theta_{ref} = -\theta_{inc} \tag{3}$$

θ_{inc} and θ_{ref} being respectively the angles of incidence and reflection with respect to the normal $\vec{n}$, (Figure 1). Thus, determining the ray’s trajectory after rebound requires knowing the impact point, the surface normal at that point, and the angle of incidence. With fixed-mesh Eulerian Level-set methods, the free interface is diffuse, and it is not possible to impose a bounce boundary condition on the metal surface. The issue is then addressed by developing an appropriate coupling between Ray tracing and Level-set.

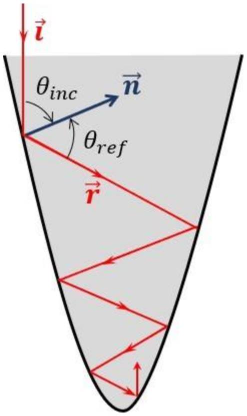

Fig. 1 Illustration of the phenomenon of multiple reflections in a cavity

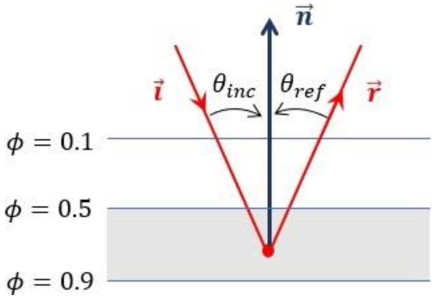

Fig. 2 Detection and reflection of a ray in the reflective layer (in light gray)

The transport equation for the Level-set variable ϕ is written as:

$$\frac{\partial \phi}{\partial t} + \vec{u}.\vec{\nabla}\phi = \gamma_{ls}\vec{\nabla}.\left(\epsilon_{ls}\vec{\nabla}\phi - \phi(1-\phi)\frac{\vec{\nabla}\phi}{|\vec{\nabla}\phi|}\right) \tag{4}$$

$\vec{u}$ is the fluid velocity (gas as liquid metal), ϵ_{ls} and γ_{ls} the numerical parameters of the Level-set method. ϕ is 1 in the metal, 0 in the gas and takes on intermediate values in the transition phase. Nevertheless, we define the isosurface $\phi = 0.5$ as the metal/gas interface. The normal at a point on this interface is calculated as:

$$\vec{n} = \frac{\vec{\nabla}\phi}{|\vec{\nabla}\phi|} \tag{5}$$

Ray tracing/Level-set coupling is achieved by defining a "reflective layer", in the metal/gas transition zone, in which the incident ray is detected and redirected (Figure 2). The reflective layer is the zone where $0.5 < \phi < 0.9$. Referring to Figure 1, an incident ray (as opposed to a reflected ray) is analytically defined by $\vec{\imath}.\vec{n} < 0$. In sum, since $\vec{\imath} \parallel \vec{V}$, any ray is reflected whenever:

$$(0.5 < \phi < 0.9) \wedge (\vec{V}.\vec{n} < 0) \tag{6}$$

and its trajectory remains linear between two consecutive points of impact.

CONSTRUCTION OF THE THERMAL SOURCE TERM

To translate reflections into energy deposits, an energy property is defined by considering that the power contained in each ray is always proportional to its velocity (Equation 7). Moreover, since the power drops after each reflection, the rebound velocity must drop in the same proportion: at the i-th reflection,

$$\frac{P_i}{V_i} = \frac{P_0}{V_0}, \quad \forall\, i = 1, \dots, N_{ref} \tag{7}$$

$$P_i = (1 - \alpha_F)P_{i-1} \Longrightarrow V_i = (1 - \alpha_F)V_{i-1} \tag{8}$$

$$(\Delta P)_i = \alpha_F P_{i-1} = \alpha_F \left(\frac{V_{i-1}}{V_0}\right) P_0 \tag{9}$$

with $\alpha_F = \alpha_F(\theta)$ the Fresnel absorptivity. V_0 is the initial ray velocity. For a laser beam of power P_{laser} discretized into N_r rays, the initial power of each ray is:

$$P_0 = \frac{P_{laser}}{N_r} \tag{10}$$

The energy deposited in the material is calculated from the power lost by the ray, Equation 9. Finally, it suffices to know, at the i-th bounce of a ray, the incident velocity and angle of incidence to define its contribution to the volume source term, Equation 11:

$$q_i = \left[\alpha_F(\theta_i)\left(\frac{V_{i-1}}{V_0}\right)\cos(\theta_i)\frac{1}{dv}\right] P_0 \tag{11}$$

with dv the volume of the mesh element containing the point of impact, $\theta_i = -\theta_{i-1} = \left|\left(\vec{n}, \vec{V_i}\right)\right|$ the angle of incidence. The bracketed term, homogeneous at m^{-3}, is calculated for all rays at each time step, directly creating a dynamic energy map of values between 0 and a maximum.

DEFINITION OF RAY EMISSION VELOCITY

Rigorously, the ray emission velocity should be taken to be equal to the speed of light in vacuum, c i.e close to the speed of light in air or metal vapour. Coupling such physics to fluid mechanics, where flows and melt penetration are characterized by velocities of the order of $\mathrm{m/s}$, would induce a numerical time-scale problem. Moreover, detecting high-speed rays through a diffuse interface would require choosing a time step such that they would not cross more than one element between t and $\mathrm{t} + \Delta\,\mathrm{t}$ (Equation 12). The conventional mesh sizes ($\mathrm{h} \sim 10 - 50\ \mu\mathrm{m}$) would then imply too small time steps.

$$\Delta t \leq \frac{h}{c} \sim 10^{-13}\, s \tag{12}$$

To overcome these obstacles, a sensitivity study was carried out on V_0 with the aim of defining an emission velocity that would allow a conceivable time step with an equally acceptable margin of error. The approach used consisted in developing a reference model where $V_0 = c$ with an ALE-type physical interface and then comparison models where $V_0 \ll$

c. The ALE not only enables all rays to be detected regardless of V_0, but also makes the tests more realistic by simulating interface deformations without solving the momentum equations. Rays are emitted into a cavity created from an initially flat interface, which deforms in three successive phases - penetration, tilting and oscillations (Figure 3)- according to the imposed velocity $\vec{v}_{inter}$:

$$\vec{v}_{inter} = \begin{cases} -v_p exp\left(-\dfrac{x^2}{{w_0}^2}\right)\vec{y}, & 0 \le t < 1 \ s \\ v_{incl}\vec{x}, & 1 \le t < 1.5 \ s \\ v_{osc} sin(2\,\pi f_{osc}\ t)\vec{y}\,, & 1.5 \le t \le 4 \ s \end{cases} \tag{13}$$

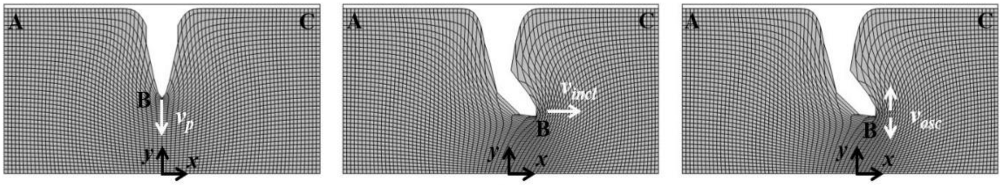

a) b) c)

Fig. 3 Free interface deformations in three phases: a) penetration, b) tilting and c) oscillations. Welding in the $-\vec{x}$ direction is assumed

Penetration velocity v_p and inclination velocity v_{incl} are estimated by analyzing X-ray images (and accompanying videos) from experiments by Wagner *et al* [11], describing the development of the keyhole in laser welding on aluminum. It emerges that these speeds are less than 1 m/s. The amplitude v_{osc} and frequency f_{osc} of the keyhole oscillation are more difficult to estimate.

In this study, we set: $v_p = v_{incl} = 1$ m/s, $v_{osc} = 0.5$ m/s and $f_{osc} = 12500$ Hz. The energy conservation equation is solved considering the properties of aluminum A2219. Mesh size and time step used: h = 50 µm and Δt = 10 µs. The irradiance profiles I_{V_0} on the free boundary during the pulse are compared for $V_0 = 1, 10, \ldots, c$. The results at 1.5 ms and 4 ms, representative of the overall observation over the entire interaction time, are shown in Figure 4.

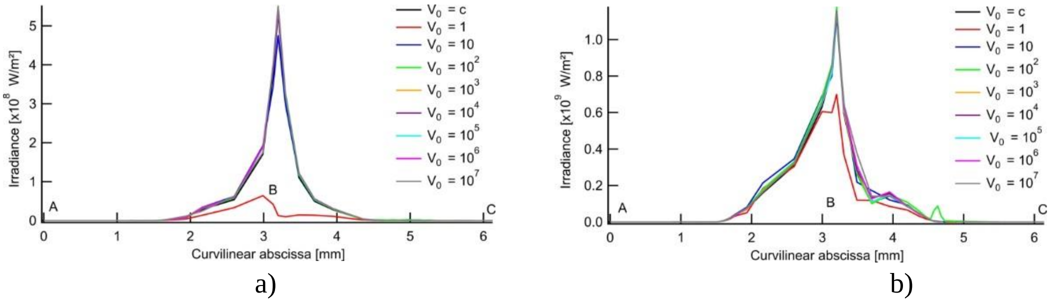

a) b)

Fig. 4 Irradiance profiles on the free boundary at a) 1.5 ms and b) 4 ms. Peaks correspond to point B, the bottom of the capillary. Laser parameters used: P_{laser} = 4 kW, w_0 = 200 µm

Figure 4 shows that only $V_0 = 1$ m/s yields a markedly different result, i.e. when rays are emitted at a speed of at least 10 m/s, the energy deposition is almost the same as if they were emitted at the speed of light. The study, repeated for emission velocities between 1 m/s and 10 m/s (V_0 = 3, 5 and 7 m/s), reveals on the one hand an abrupt deviation of irradiance peaks at point B between $I_{V_0 = 1}$ and $I_{V_0 = 3}$ and on the other hand a gradual progress towards the reference profile from $I_{V_0 = 3}$. This result suggests that the ray emission velocity is acceptable if it exceeds the characteristic velocity of the keyhole dynamics (as a reminder, v_p= 1 m/s). However, V_0 = 10 m/s will be retained to take account of uncertainties in the case of highly unstable capillaries, where characteristic velocities could be higher than those used in this numerical test.

LASER WELDING MODELING

GOVERNING EQUATIONS

The modeling of the thermohydrodynamic problem in laser welding, with free interface tracking by Level-set, is well detailed in the study by Le Mener *et al* [12]. Specific modifications to our model are mentioned here. In summary, three main conservation laws are solved to simulate heat transfer and melt flow: conservation of energy (Equation 14), conservation of momentum (Equation 15) and conservation of mass (Equation 16).

$$\rho c_{p,eq}\left[\frac{\partial T}{\partial t}+\vec{\nabla}\cdot(\vec{u}T)\right]=\vec{\nabla}\cdot\left(k\vec{\nabla}T\right)+q_{\text{laser}}-q_{\text{evap}}\delta(\phi) \tag{14}$$

$$\rho\left(\frac{\partial\vec{u}}{\partial t}+(\vec{\nabla}\vec{u}).\vec{u}\right)=\vec{\nabla}.\left[-pI+\mu\left(\left(\vec{\nabla}\vec{u}\right)+\left(\vec{\nabla}\vec{u}\right)^{T}\right)\right]+\vec{F}_v+\vec{F}_{inter}.\delta(\phi) \tag{15}$$

$$\vec{\nabla}.\vec{u} = \dot{m}\left(\frac{1}{\rho_v} - \frac{1}{\rho_l}\right)\delta_g(\phi) \tag{16}$$

In Equation 14, q_{evap} represents the energy lost through evaporation. The source term q_{laser} is the sum of the term q_i (Equation 11) over all reflections of all rays. The Fresnel absorption is written as:

$$\alpha_F(\theta) = 1 - \frac{1}{2}\left[\frac{\left(n - (1/\cos\theta)\right)^2 + k^2}{\left(n + (1/\cos\theta)\right)^2 + k^2} + \frac{(n - \cos\theta)^2 + k^2}{(n + \cos\theta)^2 + k^2}\right] \tag{17}$$

In Equation 15, F_v groups together the volume forces (buoyancy, gravity, Darcy condition) and F_{int} the surface forces (surface tension and Marangoni effect). Equation 16 includes a source term to model vaporization, representing the mass addition to the gas phase through a Dirac delta function δ_g, which ensures the incompressibility of the liquid metal:

$$\delta_g = \begin{cases} 2\delta(\phi),\ if\ \phi \leq 0.5\ \ (gas) \\ 0,\ if\ \ \phi > \ 0.5\ \ (metal) \end{cases} \tag{18}$$

Finally, the transport equation for the Level-set variable (Equation 19) is modified due to the source term added to the mass conservation equation:

$$\frac{\partial\phi}{\partial t} + \vec{u}\cdot\vec{\nabla}\phi = \dot{m}\left(\frac{1-\phi}{\rho_v} + \frac{\phi}{\rho_l}\right)\delta(\phi) + \gamma_{ls}\vec{\nabla}.\left(\epsilon_{ls}\vec{\nabla}\phi - \phi(1-\phi)\frac{\vec{\nabla}\phi}{\left|\vec{\nabla}\phi\right|}\right) \tag{19}$$

MATERIAL PROPERTIES

The temperature-dependent properties of the A2219 alloy (thermal conductivity, density and heat capacity at constant pressure) are taken from Narender *et al* [13] and Wang *et al* [14]. Given the limited data available at high temperatures, constant values are used above the melting temperature.

Three properties have been calibrated/adjusted for various reasons. The surface tension coefficient ($\sigma_0 \simeq 0.9$ N/m [15]), is reduced to 0.3 N/m for convergence reasons and above all due to the difficulty of properly modeling interface phenomena using the Level-set method. The dynamic viscosity of the liquid metal ($\mu_{liq} \simeq 10^{-3}$ Pa.s [16]) is multiplied by 100 for convergence and numerical stability of the melt pool. As the Fresnel absorption indices are not well known (literature data are often for pure aluminum, [17]), the values n = 1.75 and k = 6.5 (equivalent to an absorptivity of 14% at normal incidence and a maximum of 22% at Brewster incidence) were set to obtain molten pool dimensions close to experiment.

The thermophysical properties of the gas, a mixture of metal vapor and ambient air, are not known. Therefore, those of the air are used. Here too, the dynamic viscosity of air has been overestimated for the same reasons as for the viscosity of the metal liquid.

GEOMETRIC AND MESH CONSIDERATIONS

As a first step, a calculation in static pulse configuration is carried out using an axi-symmetrical 2D geometry (1× 3 mm^2, Figure 5a). A 10 µm quadrangular mesh is used in the area close to the axis of symmetry where the melt is expected to develop and where all physics are considered. An extension of this area, to avoid thermal edge effects, where only heat transfers in the solid are solved, is meshed in coarser triangular elements.

Then, for the weld bead model, a 3D geometry (3× 1× 2 mm^3, Figure 5b) is used and meshed using the mesh optimization technique developed by Courtois *et al* [18]. This multiple meshing technique consists of breaking down the complete model into sub-models (components), building as many as there are physics and applying a specific level of refinement to each physics according to the mesh sensitivity of the variables associated with it.

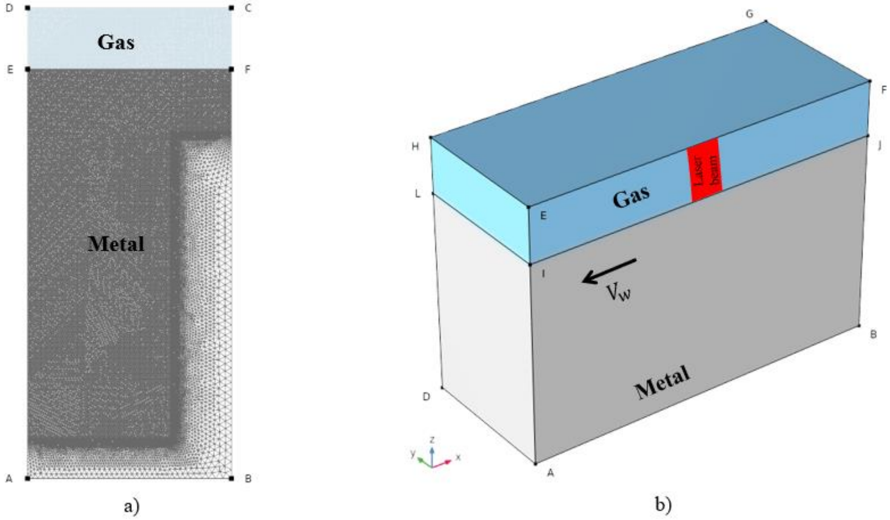

a) b)

Fig. 5 Resolution domains. a) 2D axisymmetric geometry with AD the symmetric axis. b) 3D geometry with a plane of symmetry in ABFE. The material passes under the laser source, which is held stationary

NUMERICAL SOLVER SETTINGS

The PARDISO direct solver is used to solve the equations in a segregated approach. The alpha-generalized time scheme is used with a constant time step of 0.8 µs in 2D axisymmetry and 2.8 µs in 3D. Simulations are run on a computing station with an Intel®Xeon®W-2295 processor, 3.00 GHz, 128 GB RAM, 18 cores. The static pulse simulations presented here run for up to 20 hours, including the cooling phase, whereas the weld bead model requires up to 6 days for 12 ms of the process.

VALIDATION EXPERIMENTS

Experiments were carried out with the TRUMPF disk laser, Trudisk 6001, wavelength $\lambda = 1030$ nm. PRIMES' FocusMonitor FM+ laser beam analyzer was used to determine beam characteristics (energy distribution, quality factor, focal plane radius, Rayleigh length). The temporal profile of laser power was also measured. The laser beam was slightly inclined to avoid reverse reflections in the optical cavity. All tests were carried out without the addition of shielding gas.

Static laser shots were performed on 4 mm-thick A2219 alloy plates at the focal plane ($z = 0$), where the beam radius is $w_0 = 150\,\mu m$. Each configuration was repeated multiple times to assess experimental variability. The weld bead presented here was obtained using a laser power of $P_{\text{laser}} = 2\ \text{kW}$, a welding speed $V_w = 10\ \text{m/min}$, and a focal position set at 0.

RESULTS

STATIC PULSES

The static shot models are compared with experimental results after solidification. The comparison concerns the dimensions (penetration depth and diameter) of the melted zone and checks for the presence of porosity. Figures 6a-c show the experimental melt pool morphology for different laser parameters, while Figures 6d-f present the corresponding numerical results.

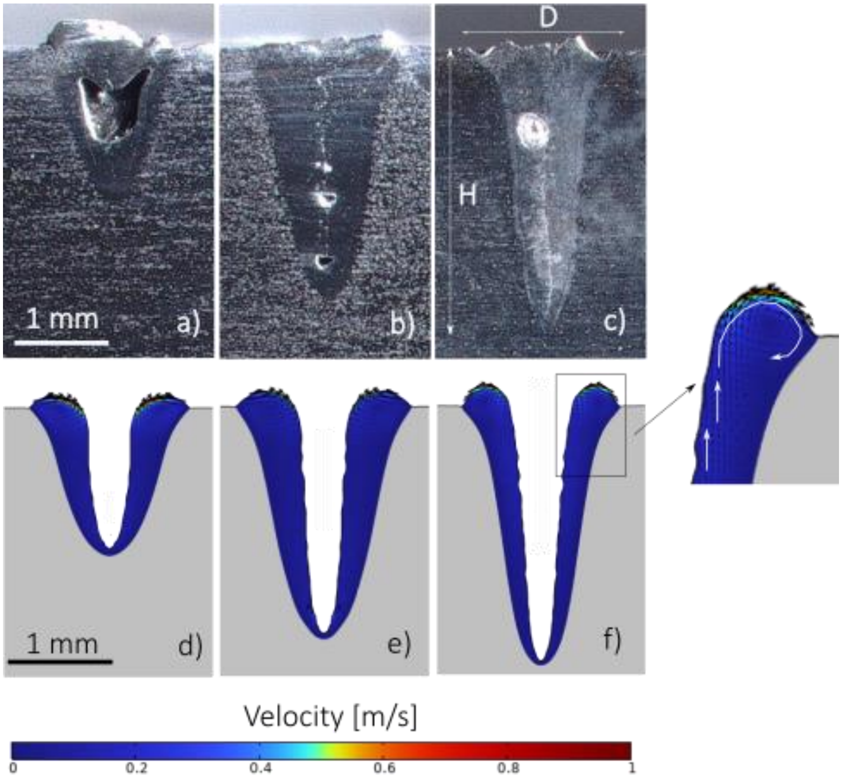

Fig. 6 Morphology of experimental and numerical melt zones. The experimental results are post-mortem, whereas the numerical results correspond to the melt pool during the laser pulse. H and D represent melt zone depth and diameter respectively. Laser parameters: a) and d) P_{laser} = 2 kW, t_{pulse} = 4 ms, b) and e) P_{laser} = 3 kW, t_{pulse} = 4 ms, c) and f) P_{laser} = 4 kW, t_{pulse} = 2 ms

A notable observation is the presence of residual porosities in the three welds shown (also observed in most other welds not displayed here). This confirms literature reports on the difficulty of determining laser parameter sets that allow porosity -free welds on aluminum. Moreover, the model successfully reproduces the shape of the molten zone.

The calculated flow velocities in the melt pool do not exceed 1 m/s. Although experimental measurements were not carried out, the overestimation of dynamic viscosity in the model should theoretically lead to underestimated numerical velocities. Nonetheless, the flow direction, from inside the keyhole toward the fusion front (Figure 6f), is consistent with the negative sign of the thermocapillary coefficient.

The model predicts the penetration depth and diameter of the molten zone with maximum errors of 38 % and 24 %, respectively, compared to experiments (Figure 7). Repeating the pulses revealed significant variability in some cases, for instance, with P_{laser} = 2 kW and t_{pulse} = 6 ms, where a 62 % difference was noted between two measured depths. These penetration variations, observed under identical power and pulse duration, may result from local oxidation differences, which affect absorptivity. In addition, cutting techniques may introduce measurement uncertainty when locating the exact center of the laser spot.

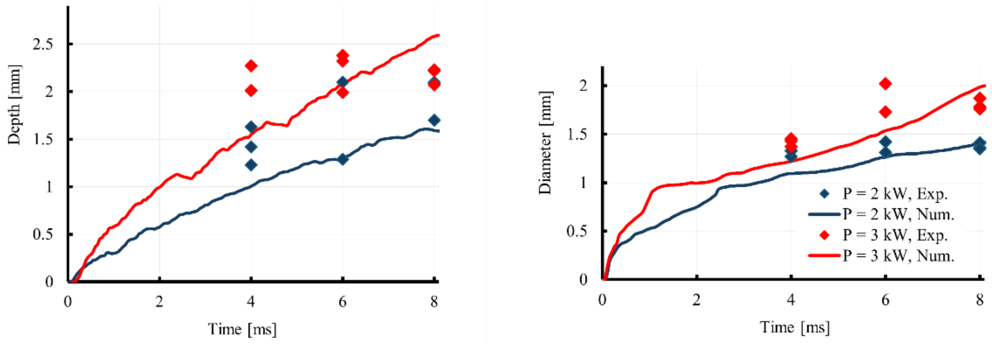

Fig. 7 Model/experiment comparison of the evolution of dimensions (depth on the left and diameter on the right) of melted zones for $P_{laser} = 2$ kW and $P_{laser} = 3$ kW

Since a central objective of this work is to develop a new method for describing laser–material interaction (LMI), it is crucial to discuss the consistency of the energy balance by quantifying the absorbed energy and its impact on keyhole formation and development. Figure 8 illustrates the LMI in different process stages, from an undeformed metallic surface to a deep keyhole.

In the initial stage (before 100 µs), the metal melts but the molten pool surface remains undeformed. The first rays bounce off, nearly retracing their incoming trajectories (Figure 8a). This pure conduction regime lasts barely 0.2 ms, until the vaporization temperature is reached and the surface begins to curve. At this point, rays still reflect after a single bounce but deviate noticeably from their initial paths (Figure 8b). Multiple reflections start to occur around 0.4 ms, when the keyhole aspect ratio (depth/diameter) reaches 0.8. The keyhole then deepens and narrows progressively, trapping many rays at its bottom.

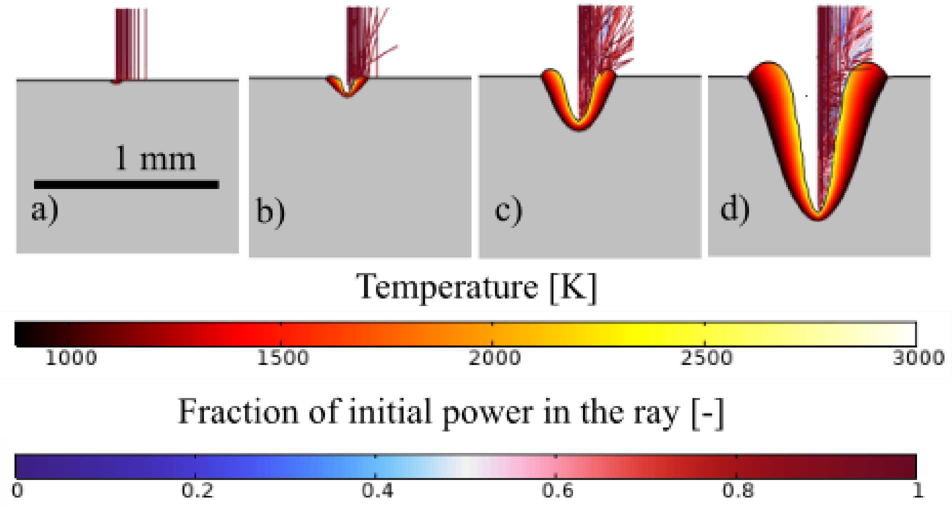

Fig. 8 Illustration of multiple reflections inside the capillary and temperature field in the melt at a) 0.1 ms, b) 0.2 ms, c) 0.6 ms and d) 2.1 ms for P_{laser} = 2 kW, w_0 = 150 µm

The absorptance evolution (absorbed power relative to laser power) over time is plotted in Figure 9, compared with the analytical model of Gouffé [5]. In static pulses, since the keyhole remains relatively regular, knowing its depth and opening diameter at each instant allows plotting the Gouffé profile. The numerical model closely follows both the trend and values of the analytical model, providing further confirmation of the consistency of our method for energy deposition.

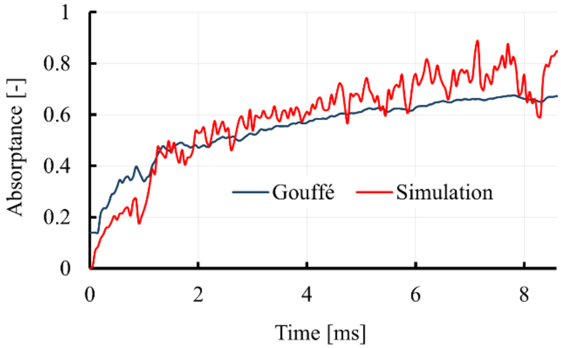

Fig. 9 Time evolution of calculated absorptance and comparison with Gouffé's analytical prediction. P_{laser} = 2 kW, w_0 = 150 µm

FUSION LINE

Given the good results obtained in the static configuration, the model was upgraded to a 3D fusion line model. No major changes were necessary, except for the meshing technique and the relative movement between the laser source and the material. Various views of the melt pool are shown in Figure 10.

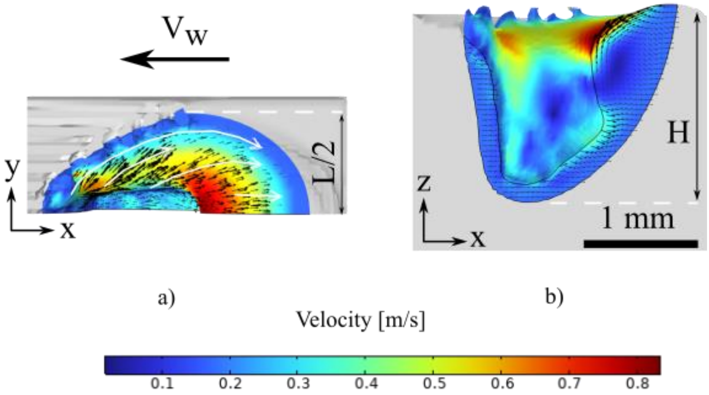

Fig. 10 Numerical result after 12 ms. a) Top view and velocity field at the surface of the weld pool. Oriented white lines indicate overall flow direction. b) Side view and velocity field in the melt. P_{laser} = 2 kW, w_0 = 150 µm, V_w = 10 m/min

The steady state is defined as the final phase of the process, during which the main fields - temperature, velocity, and pressure - show no significant variation. From a macroscopic perspective, the penetration depth reaches a maximum and then oscillates around a mean value. To ensure this regime is attained, numerical results must be analyzed over several tens of milliseconds. However, as this numerical model is still under development, the present simulations are limited to 12 ms and need to be extended to yield fully reliable results. Nonetheless, some indicators suggest that a steady-state regime has at least begun by this point:

- for V_w = 10 m/min, a 2 mm-long weld bead has already formed after 12 ms of laser–material interaction.
- As will be shown later, the keyhole shape at 12 ms exhibits distinct characteristics.

As previously mentioned, simulations will need to be extended to longer process times and repeated for different laser powers and welding speeds before any conclusions can be drawn regarding its robustness. Nevertheless, preliminary analyses of keyhole dynamics are already possible. The dynamics illustrated in Figure 12 over the 12 ms simulation display consistent trends that are worth noting.

Up to 3 ms, the keyhole remains symmetric, the molten zone is roughly balanced on both sides, and the internal surface temperature, except near the solidification front, remains uniform, much like in static pulse conditions. Starting from 4 ms, the front and rear sides begin to differ as molten metal accumulates at the rear. In addition, temperature fields become increasingly non-uniform (as seen at 10 ms and 11 ms): the front and bottom of the keyhole, directly exposed to the laser, are hotter than the rear and lateral surfaces, which are heated only by reflected laser radiation. By 12 ms, the lower part of the keyhole, whose bulging started at 10 ms, expands further in a direction opposite to the welding movement, while the upper part tends to narrow.

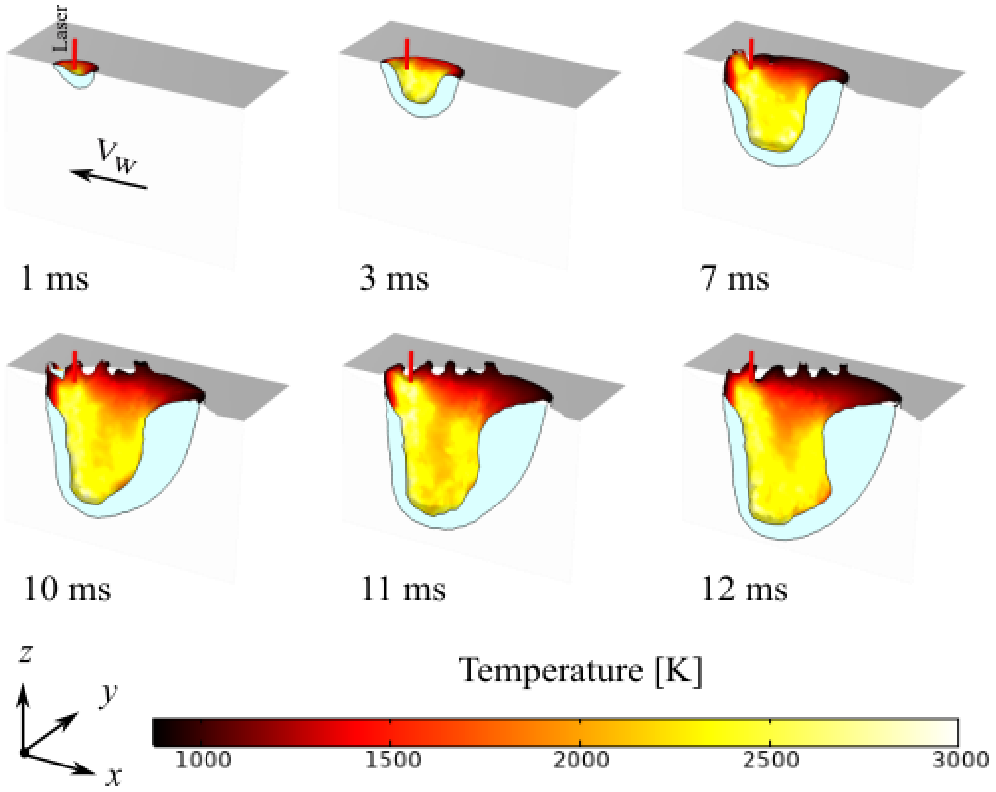

Fig. 12 Evolution of keyhole geometry and temperature field. The melted volume is shown in light blue. P_{laser} = 2 kW, w_0 = 150 µm, V_w= 10 m/min

CONCLUSIONS AND OUTLOOK

The objective of this work was to study keyhole instabilities and related defects during laser welding of aluminum. To better account for multiple laser beam reflections, a new method based on ray tracing was developed and applied to both static pulse and fusion line configurations. The main findings are summarized as follows:

- Our approach offers an innovative way to simplify high-fidelity simulation of melt pool dynamics within commercial software, while reducing computation time.
- In static pulse conditions, the energy deposition predicted by this approach agrees with Gouffé's theory, and the simulated molten zones exhibit morphological features (size, porosity presence) consistent with experimental observations.
- The fusion line model, although still under development, shows initial results that suggest promising potential.

Further calculations will be required to obtain fully conclusive results. Complete model validation will also necessitate additional experimental investigations, including flow visualization, keyhole deformation tracking. Finally, we intend to explore beam shaping strategies to improve process stability and reduce porosity formation.

References

[1] A. MATSUNAWA, M. MIZUTANI, S. KATAYAMA and N. SETO: 'Porosity formation mechanism and its prevention in laser welding', *Weld. Int.*, vol. 17, no. 6, pp. 431-437, Jun. 2003, doi: 10.1533/wint.2003.3138.

[2] A. MATSUNAWA, J.-D. KIM, N. SETO, M. MIZUTANI and S. KATAYAMA: 'Dynamics of keyhole and molten pool in laser welding', *J. Laser Appl.*, vol. 10, no. 6, pp. 247-254, Dec. 1998, doi: 10.2351/1.521858.

[3] W. KE, X. BU, J. P. OLIVEIRA, W. XU, Z. WANG and Z. ZENG: 'Modeling and numerical study of keyhole-induced porosity formation in laser beam oscillating welding of 5A06 aluminum alloy', *Opt. Laser Technol.*, vol. 133, p. 106540, Jan. 2021, doi: 10.1016/j.optlastec.2020.106540.

[4] F. FETZER, C. HAGENLOCHER, R. WEBER and T. GRAF: 'Geometry and stability of the capillary during deep-penetration laser welding of AlMgSi at high feed rates', *Opt. Laser Technol.*, vol. 133, p. 106562, 2021.

[5] A. GOUFFÉ: 'Corrections d'ouverture des corps noirs artificiels compte tenu des diffusions multiples internes', *Rev. Opt.*, 1945.

[6] M. COURTOIS, M. CARIN, P. L. MASSON, S. GAIED and M. BALABANE: 'A new approach to compute multi-reflections of laser beam in a keyhole for heat transfer and fluid flow modelling in laser welding', *J. Phys. Appl. Phys.*, vol. 46, no. 50, p. 505305, Dec. 2013, doi: 10.1088/0022-3727/46/50/505305.

[7] J. DALIGAULT, M. DAL, C. GORNY, F. COSTE and R. FABBRO: 'Combination of Eulerian and ray-tracing approaches for copper laser welding simulation', *J. Laser Appl.*, vol. 34, no. 4, p. 042042, Nov. 2022, doi: 10.2351/7.0000786.

[8] L. WESTHOFEN ET AL.: 'Ray tracing method with implicit surface detection for smoothed particle hydrodynamics-based laser beam welding simulations', *Mater. Werkst.*, vol. 55, no. 1, pp. 40-52, Jan. 2024, doi: 10.1002/mawe.202300161.

[9] J. LIND, F. FETZER, D. BLAZQUEZ-SANCHEZ, J. WEIDENSDÖRFER, R. WEBER and T. GRAF: 'Geometry and absorptance of the cutting fronts during laser beam cutting', *J. Laser Appl.*, vol. 32, no. 3, p. 032015, Jun. 2020, doi: 10.2351/7.0000024.

[10] Y. A. MAYI, M. DAL, P. PEYRE, M. BELLET and R. FABBRO: 'Physical mechanisms of conduction-to-keyhole transition in laser welding and additive manufacturing processes', *Opt. Laser Technol.*, vol. 158, p. 108811, Feb. 2023, doi: 10.1016/j.optlastec.2022.108811.

[11] J. WAGNER, C. HAGENLOCHER, M. HUMMEL, A. OLOWINSKY, R. WEBER and T. Graf: 'Synchrotron X-ray Analysis of the Influence of the Magnesium Content on the Absorptance during Full-Penetration Laser Welding of Aluminum', vol. 11, no. 5, p. 797, 2021, doi: 10.3390/met11050797.

[12] M. LE MENER, M. COURTOIS, N. DAVIOT, M. CARIN and R. ANDRY: 'Heat transfer and fluid flow modeling of steel-Inconel laser welding in an overlap configuration', *J. Laser Appl.*, vol. 36, no. 4, p. 042006, Nov. 2024, doi: 10.2351/7.0001357.

[13] K. NARENDER, A. S. M. RAO, K. G. K. RAO and N. G. KRISHNA: 'Thermo physical properties of wrought aluminum alloys 6061, 2219 and 2014 by gamma ray attenuation method', *Thermochim. Acta*, vol. 569, pp. 90-96, Oct. 2013, doi: 10.1016/j.tca.2013.07.003.

[14] H. X. WANG, Y. H. WEI and C. L. YANG: 'Numerical simulation of variable polarity vertical-up plasma arc welding process', *Comput. Mater. Sci.*, vol. 38, no. 4, pp. 571-587, Feb. 2007, doi: 10.1016/j.commatsci.2006.03.017.

[15] Y. ZHANG, Z. SHEN and X. NI: 'Modeling and simulation on long pulse laser drilling processing', *Int. J. Heat Mass Transf.*, vol. 73, pp. 429-437, Jun. 2014, doi: 10.1016/j.ijheatmasstransfer.2014.02.037.

[16] A. T. DINSDALE and P. N. QUESTED: 'The viscosity of aluminium and its alloys–A review of data and models', *J. Mater. Sci.*, vol. 39, no. 24, pp. 7221-7228, Dec. 2004, doi: 10.1023/B:JMSC.0000048735.50256.96.

[17] W. M. STEEN and J. MAZUMDER: *Laser Material Processing*, London: Springer London, 2010, doi: 10.1007/978-1-84996-062-5.

[18] M. COURTOIS, M. CARIN, P. L. MASSON, S. CADIOU and S. GAIED: 'A method to reduce calculation time in multiphysic modelling of welding processes. Application to laser and GMAW welding.', 2019.